We are IntechOpen,
the world's leading publisher of
Open Access books
Built by scientists, for scientists

4,800
Open access books available

122,000
International authors and editors

135M
Downloads

Our authors are among the

154
Countries delivered to

TOP 1%
most cited scientists

12.2%
Contributors from top 500 universities

CLARIVATE ANALYTICS
BOOK CITATION INDEX
INDEXED

WEB OF SCIENCE™

Selection of our books indexed in the Book Citation Index
in Web of Science™ Core Collection (BKCI)

Interested in publishing with us?
Contact book.department@intechopen.com

Numbers displayed above are based on latest data collected.
For more information visit www.intechopen.com

Al$_2$O$_3$-enhanced Macro/Mesoporous Fe/TiO$_2$ for Breaking Down Nitric Oxide

Dieqing Zhang and Guisheng Li

Department of Chemistry, Key Laboratory of Resource Chemistry of
Ministry of Education, Shanghai Normal University, Shanghai 200234,
China

1. Introduction

High air contaminant levels in the indoor environment come from either the ambient air or from indoor sources. (Cao, 2001) Nitrogen oxide is one of the most common gaseous pollutants found in the indoor environment with the concentration in the range of 70-500 parts-per-billion (ppb) levels. This has serious implications on the environment and health of the mankind. (Huang et al., 2009) Conventional techniques to treat nitric oxide in industrial emission mainly include physical adsorption, biofiltration, and thermal catalysis methods. However, these methods usually suffer from some disadvantages, such as the low efficiency for pollutants at the parts per billion level and the difficulty in solving the postdisposal and regeneration problems. (Huang et al., 2008)

As a promising environmental remediation technology, semiconductor-mediated photocatalytic technology has been widely used to purify contaminated air and wastewater. (Fox & Dulay, 1993) Titanium dioxide is the most widely used photocatalyst because of its superior photoreactivity, nontoxicity, long-term stability and low price. Recently, great attention has been paid to macro/mesoporous TiO$_2$ for its interconnected macroporous and mesoporous structures. Such hierarchical material may enhance properties compared with single-sized pore materials due to increased mass transport through the material and minimized pressure drop over the monolithic material.(Yuan et al. 2006) Meanwhile the macroporous channels could serve as light-transfer paths for the distribution of photon energy onto the large surface of inner photoactive mesoporous frameworks. Therefore, higher light utilization efficiency could be obtained for heterogeneous photocatalytic systems including photooxidation degradation and solar cells. In addition, the hierarchical structure-in-structure arrangement of mesopore and macropore is benefit for the molecule traffic control and for the resistance of the photocatalyst to poisoning by inert deposits.(Rolison 2003)

Though such structure contributes great advantages to TiO$_2$, such as a readily accessible pore-wall system and better transport of matter compared to the traditional TiO$_2$ photocatalysts, the anatase TiO$_2$ semiconductor has a relatively large band gap of 3.2 eV, corresponding to a wavelength of 388 nm.(Yu et al., 2006) The requirement of UV excitation impedes the development of solar-driven photocatalytic systems. As a promising way, doping method can effectively extend the light absorption of TiO$_2$ to the visible region and reduce the recombination of photoinduced electrons and holes.(Zhu et al., 2007) Among

various dopants, the Fe^{3+}-dopant is most frequently employed owing to its unique half-filled electronic configuration, which might narrow the energy gap through the formation of new intermediate energy levels and also diminish recombination of photoinduced electrons and holes by capturing photoelectrons. However, calcination of the photocatalysts at high temperature is usually indispensable for removing organic templates, enhancing structural crystallization, and allowing doped ions to enter into the frameworks of TiO_2.(Wang et al., 2009) Such treatment at high temperature will result in great loss of surface area and destroying the pore systems owing to the grain growth, especially for porous materials. Thus, the photoactivity of the calcined samples with low specific area will be greatly reduced for the poor light-harvesting capability.(Yu et al., 2006) Fortunately, using inorganic structure stabilizers (SiO_2, ZrO_2, and Al_2O_3) could allow the anti-sintering properties of porous materials to be promoted greatly enough for application in high temperature environment, such as treating automotive exhaust.(Wang et al., 1999)

In this chapter, we describe a detailed study of the effect of Al_2O_3 as a promoter in enhancing a macro/mesoporous visible-light photocatalyst, Fe/TiO_2, for the oxidation of nitric oxide (NO). The photocatalysts are synthesized through directing the formation of inorganic phases (Al_2O_3-Fe/TiO_2) with multidimensional pore systems through the self-assembly of a single surfactant under hydrothermal conditions. The experimental results showed that doping Fe^{3+} into the framework of TiO_2 can effectively extend the optical absorption spectrum to visible light range. Introducing highly dispersed amorphous Al_2O_3 species into the Fe/TiO_2 system could greatly increased the thermal stability of the Fe/TiO_2 framework with higher surface area and larger pore volume. It is surprising that the Al_2O_3-Fe/TiO_2 sample treated at 700 °C possessed a high specific surface area (ca. 130 m^2/g), about 6 times of that of the Al_2O_3-free sample. The photooxidation of NO in air over the 3D macro/mesoporous Al_2O_3-Fe/TiO_2 photocatalysts was studied. These products were utilized to remove gaseous NO at 400 parts-per-billion level in air under visible-light irradiation. These Al_2O_3-Fe/TiO_2 photocatalysts exhibited very strong ability to oxidize the NO gas in air under visible-light irradiation. Importantly, these 3D macro/mesoporous Al_2O_3-Fe/TiO_2 photocatalysts showed excellent stability and maintained a high level of photocatalytic activity after multiple reaction cycles.

2. Experiment section

2.1 Preparation of 3D macro/mesoporous Al_2O_3-Fe/TiO_2 photocataltsts

Brij 56 [$C_{16}(EO)_{10}$], titanium isopropoxide, aluminum sec-butoxide, and ferric (III) nitrate are purchased from Aldrich. All chemicals were used as received. In a typical synthesis of macro/mesoporous visible light photocatalysts Al_2O_3-Fe/TiO_2, required amount of ferric (III) nitrate was dissolved in a aqueous solution of Brij 56 (15 wt %) with pH = 2 adjusted by sulfuric acid under ultrasonic irradiation in an ultrasonic clean bath (Bransonic ultrasonic cleaner, model 3210E DTH, 47 kHz, 120 W, USA). 18 ml mixture of aluminum sec-butoxide and titanium isopropoxide with a metal-to-metal molar ratio (M_{Al}/M_{Ti} = 20:100) was added drop by drop into the above medium under stirring, followed by further stirring for 0.5 h. The obtained mixture was then transferred to a Teflon-lined autoclave and heated at 80 °C for 36 h under static condition during which the inorganic precursor hydrolyses and polymerizes into a metal oxide network. Finally, the as-prepared white samples were clacined at 400-700 °C for 8 h at 1 °C/min to remove the surfactant species and improve the crystallinity. The as-prepared Al_2O_3-Fe/TiO_2 samples were denoted as Al-Fe/TiO_2-400, Al-

Fe/TiO$_2$-500, Al-Fe/TiO$_2$-600 and Al-Fe/TiO$_2$-700, where 400-700 refers to the calcinations temperature. For comparation, macro/mesoporous photocataltsts, pure TiO$_2$ and Fe/TiO$_2$, were also prepared by the same procedure. The molar ratio of Fe/Ti is 0.25 % for all the Fe doped samples.

2.2 Characterization

X-ray diffraction (XRD) measurements were carried out using a Bruker D8 Advance X-ray diffractometer (Cu Kα$_1$ irradiation, λ = 1.5406 Å) at a scanning rate of 0.02 Degree/Second. The Schrerrer equation ($\Phi = K\lambda/\beta cos\theta$) was used to calculate the crystal size.(Machida, Norimoto et al. 1999) In the above equation, λ (0.154 nm) is the wavelength of the X-ray irradiation, K is a constant of 0.89, $β$ is the peak width at half-maximum height after subtraction of the instrumental line broadening using silicon as a standard, and 2θ = 25.3 º and 2θ = 27.4 º for anatase and rutile. The phase composition was estimated using the following equations: rutile % = 100 × (0.884A/R + 1)$^{-1}$,(Machida, Norimoto et al. 1999) where A is the peak area of anatase (101) and R is the peak area of rutile (110). The intensity of both of the two peaks is the most intense reflection in the diffractograms. The number of 0.884 is the coefficient of scattering. The morphology and the surface roughness of as-prepared samples were examined by a LEO 1450 VP scanning microscope. Standard transmission electron microscopy images were recorded using a CM-120 microscope (Philips, 120 kV). High-resolution transmission electron microscopy (HRTEM) was recorded in JEOL-2010F at 200 kV. A trace amount of sample was suspended in ethanol solution. After sonication for 10 min, carbon-coated copper grids were used to hold the samples followed by drying. Nitrogen adsorption-desorption isotherms were analyzed at 77 K using Micromeritics ASAP 2010 equipment. The reflectance spectra of the samples over a range of 200-700 nm were recorded by a Varian Cary 100 Scan UV-vis system equipped with a Labsphere diffuse reflectance accessory. Labsphere USRS-99-010 was employed as a reflectance standard. FT-IR spectra on pellets of the samples mixed with KBr were recorded on a Nicolet Magna 560 FT-IR spectrometer.

2.3 Photocatalytic activity testing

The photocatalytic experiments for the removal of NO gas in air were performed at ambient temperature in a continuous flow rectangular reactor (10 H cm*30 L cm*15Wcm). A 300Wcommercial tungsten halogen lamp (General Electric) was used as the simulated solar light source. A piece of Pyrex glass was used to cut off the UV light below 400 nm. Four minifans were used to cool theflowsystem. Photocatalyst (0.2 g) was coated onto a dish with a diameter of 12.0 cm. The coated dish was then pretreated at 70 ºC to remove water in the suspension. The NO gas was acquired from compressed gas cylinder at a concentration of 48 ppm NO (N$_2$ balance, BOC gas) with traceable National Institute of Stands and Technology (NIST) standard. The initial concentration of NO was diluted to about 400 ppb by the air stream supplied by a zero air generator (Thermo Environmental Inc. model 111). The desired humidity level of the NO flow was controlled at 70% (2100 ppmv) by passing the zero air streams through a humidification chamber. The gas streams were premixed completely by a gas blender and the flow rate was controlled at 4 L.min-1 by a mass flow controller. After the adsorption-desorption equilibrium among water vapor, gases and photocatalysts was achieved, the lamp was turned on. The concentration of NO was continuously measured by a chemiluminescence NO analyzer (Thermo Environmental Instruments Inc. model 42c), with a sampling rate of 0.7 L/min.

3. Results and discussion

3.1 X-ray diffraction and N_2 sorption

The crystal composition, thermal stability and mesoporous structure of the as-prepared samples were investigated by X-ray diffraction (XRD) and N_2 sorption analyses. Figure 1a shows the wide-angle XRD patterns of the Fe-doped TiO_2 calcined at different temperatures. For the 400 °C sintering sample, a broad peak corresponding to (101) diffraction of anatase-TiO_2 (JCPDS 21-1272) was observed. The broadening of the diffraction peak may have been caused by the small crystalline grain size (6.1 nm). Upon increasing the temperature to 500 °C, the intensity of this peak became stronger and sharper, indicating that larger particles (8.0 nm) were formed. However, when the calcination temperature was increased to 600 °C, the intensity of the anatase-TiO_2 diffraction peak decreased. Meanwhile, weak peaks indexable as diffractions of rutile-TiO_2 (JCPDS 87-920) appeared. About 4.5 % of the anatase-TiO_2 was converted to rutile-TiO_2.
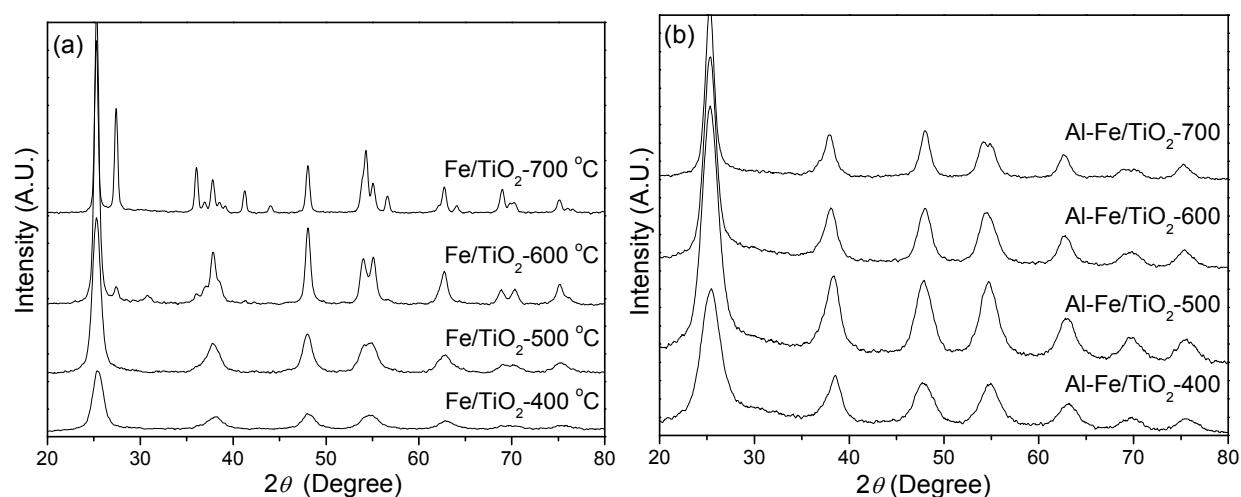

Fig. 1. XRD patterns of the as-prepared Fe/TiO_2 and $Al-Fe/TiO_2$ samples calcined at different temperatures.

After calcinations at 700 °C, the size of anatase-TiO_2 increased dramatically to 20.0 nm, and nearly 43.3 % of the anatase-TiO_2 was converted to rutile-TiO_2. Nevertheless, introducing Al_2O_3 species into the Fe-doped TiO_2 system greatly inhibited the crystal growth and the phase-transition. As shown in Figure 1b, all of the Al_2O_3 modified Fe/TiO_2 samples exhibited pure anatase phase at different temperatures. More interestingly, the crystal size of the anatase TiO_2 was greatly decreased after modifying Al_2O_3. Even after 700 °C calcination, the grain size can be maintained about 7.2 nm, much smaller than that (20.0 nm) of Fe/TiO_2 sample calcined at 700 °C. These wide-angle XRD results revealed that thermal treatment induced the growth of crystal size and subsequent phase transition could be effectively prohibited by doped Al_2O_3 species acting as structural agents. As known, thermal-induced changes in crystal composition and size also had remarkable effects on the textural properties of TiO_2 framework. N_2 sorption analyses were utilized to confirm the change of textural properties.
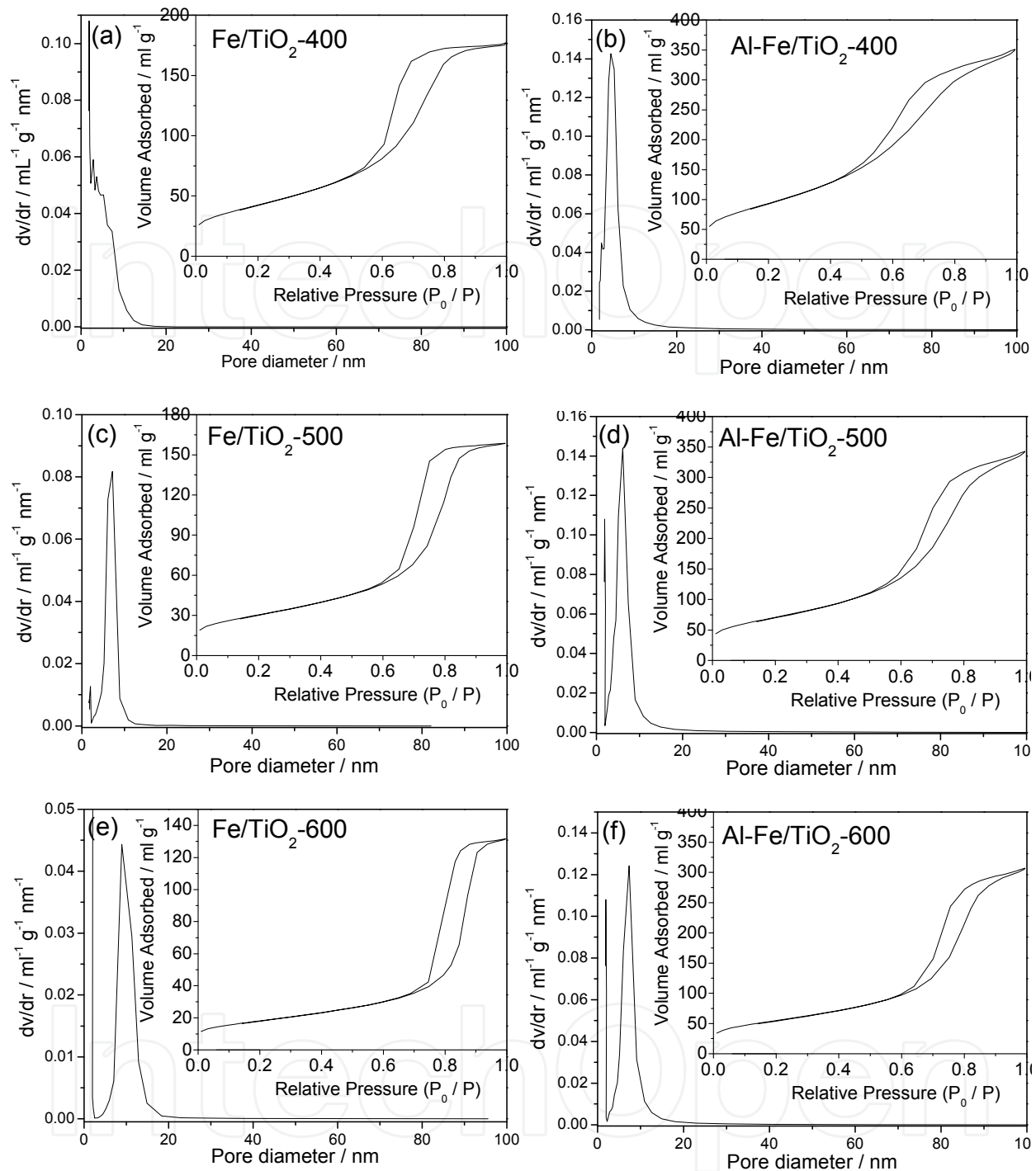
Fig. 2. N₂ adsorption-desorption isotherms (a, c, and e) and pore size distributions (b, d, and f) of the as-prepared Fe/TiO₂ and Al-Fe-TiO₂ samples calcined at different temperatures.

N₂ sorption analyses were utilized to investigate the change of textural properties of the as-prepared products. Figure 2 shows the N₂ sorption isotherms and pore size distributions for the modified titanium dioxide calcined at different temperatures. Upon 400 °C calcinations, both of Fe/TiO₂-400 and Al-Fe/TiO₂-400 samples exhibited stepwise adsorption and desorption (type IV isotherms) as shown in Figure 2a and b, indicative of a typical mesoporous structure within the as-prepared samples. As shown in Table 1, Al-Fe/TiO₂-400

sample possesses a surface area of 340.0 m²/g, much higher than that (153.6 m²/g) of Fe/TiO₂-400 owing to the anti-agglutination effect of induced Al_2O_3 species. The modification of Al_2O_3 also contributed a super lager pore volume (0.53 cm³/g) to Al-Fe/TiO₂-400 sample. It is about two times of that (0.27 cm³/g) of Fe/TiO₂-400. Such high surface area and large pore volume will make this material an excellent photocatalyst for its strong adsorption capability. With increase the calcinations temperature, the mesoporous structure of Fe/TiO₂ sample was destroyed. When the calcinations temperature was increased to 700 ºC, the surface area was decreased to 22.6 m²/g, and the pore volume was decreased to 0.11 cm³/g. This is an indication of the collapse of the pore. However, Al-Fe/TiO₂ still owns a high surface area of 131.8 m²/g and pore volume of 0.44 cm³/g. To the case of the pore-size distribution, the modification of Al_2O_3 also inhibited the pore size changing owing to its porous structure-stabilizing capability.

Sample	Surface Area/m²/g[a]	Pore Volume/mL/g[b]	Pore Size/nm[c]	Rutile content/Wt %	Crystal Size/nm[d]
Fe/TiO₂-400	153.6	0.27	5.9	0	6.1
Fe/TiO₂-500	109.5	0.24	7.6	0	8
Fe/TiO₂-600	64.9	0.20	11.3	4.5	13.4
Fe/TiO₂-700	22.6	0.11	31.2	43.3	20.0
Al-Fe/TiO₂-400	340.0	0.53	5.3	0	3.2
Al-Fe/TiO₂-500	254.7	0.52	6.8	0	4.0
Al-Fe/TiO₂-600	197.1	0.46	8.1	0	5.3
Al-Fe/TiO₂-700	131.8	0.44	12.4	0	7.2

[a] BET surface area is calculated from the linear part of the BET plot (p/p_0 = 0.1-0.2).[b] The total pore volumes are estimated from the adsorbed amount at a relative pressure of p/p_0 = 0.99.[c] The pore-size distributions (PSD) are derived from the adsorption branches of the isotherms by using the Barrett-Joyner-Halenda (BJH) method.[d] Crystal size was calculated based on XRD results.

Table 1. Textural properties and crystalline structures and of the prepared porous samples.

3.2 Scanning Electron Microscopy (SEM)

The N₂ sorption analyses could provide mesoporous structure information of the as-prepared materials. To the case of the macroscopic properties, scanning electron microscopy (SEM) should be utilized to examine the macrostructure of the modified TiO₂ monolithic particles. Meanwhile, the high-resolution state of SEM images could also give information on the mesoscopic properties. As shown in Figure 3a, Al-Fe/TiO₂-400 is typically in a large monolithic form (> 30 µm), and exhibits macroscopic network structure with relatively homogeneous macropores of 1~2 µm (size) and about 20 µm (length) in dimension as shown Figure 3b. It is more interesting that these ultralong macroscopic channels are arranged parallel to each other. Figure 3b also demonstrates the extension of the parallel-arrayed macropores completely through the material from the side view of the sample. Such open-ended tubelike macrochannels could serve as ideal light-transport routes for introducing

more photoenergy into the interior of the framework of TiO$_2$. Meanwhile, the high-resolution SEM images (Figure 3c) shows that the walls of the macroporous TiO$_2$ frameworks are composed of small interconnected TiO$_2$ particles. The mesoporous structure of the as-prepared materials is probably partly due to the intraparticle porosity and partly due to the interparticle porosity of these fine particulates.(Wang, Yu et al. 2005) The macro/mesoporous structure nearly can be maintained even after 600 ^{o}C calcinations.
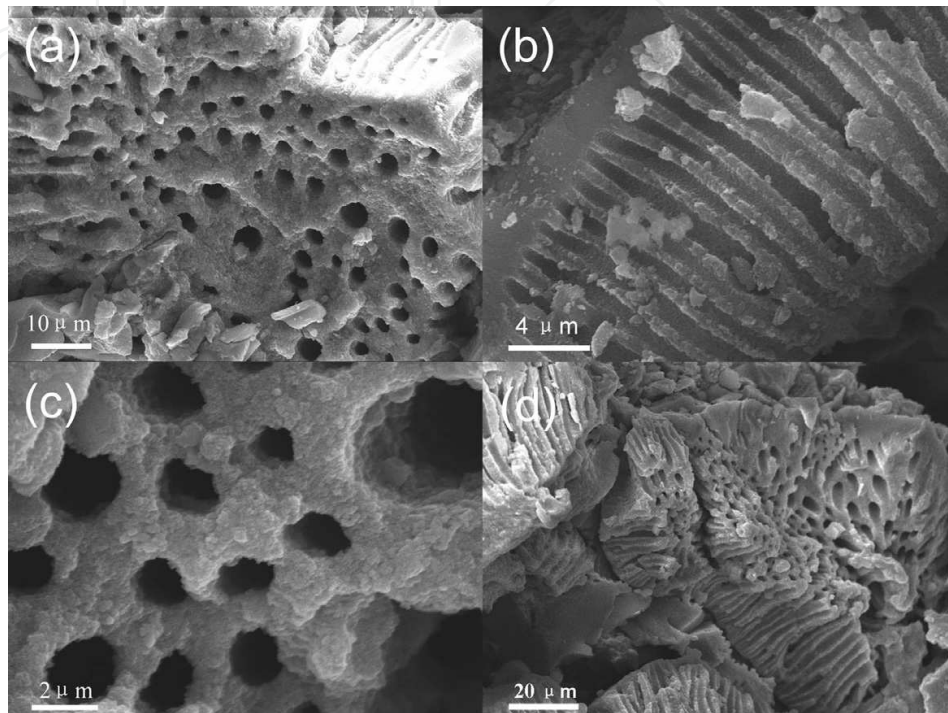
Fig. 3. SEM images of the Al-Fe/TiO$_2$ samples calcined at 400 °C (a, b, c), and 600 °C (d).

3.3 UV-vis spectra

UV-visible diffuse reflectance spectroscopy (DRS) was utulized to investigate the electronic states of the as prepared samples. Figure 4a shows the UV-visible absorption spectra of TiO$_2$-400, Fe/TiO$_2$-400, Al-Fe/TiO$_2$-400 and Al-Fe/TiO$_2$-700 samples. For large energy gap of anatase (3.2 eV), TiO$_2$-400 sample has no significant absorbance for visible-light. Upon doping Fe^{3+} ions, the light absorption edge of Fe/TiO$_2$-400 sample was extended to visible light region (λ < 650 nm) attributed to the formation of Fe-intermediate energy levels, resulting in a decrease in the energy band. The other three samples exhibit a broad absorption bands from 200 to 600 nm with respect to the pure TiO$_2$, indicating the effective photo-absorption property for this macro/mesoporous structure oxide composite photocatalyst system. This is because Fe-doping induces the absorbance for visible light owing to, leading to a decrease in the energy band gap.(Nahar, Hasegawa et al. 2006)

Compared to Fe/TiO$_2$-400 sample, Al-Fe/TiO$_2$ shows a higher light-absorbance ability located in 200~400 nm. This is because the macro/mesoporous structure, enlarged surface area and multiple scattering enable it to harvest light much more efficiently.(Yu, Wang et al. 2004) This enhanced light-trapping effect is the result of the reflection or transmission of the light scattered by the macroporous tunnels or mesopores implanted in the body of Al, Fe co-doped TiO$_2$ matrix. It is also noted that the modification of Al$_2$O$_3$ did not change the light
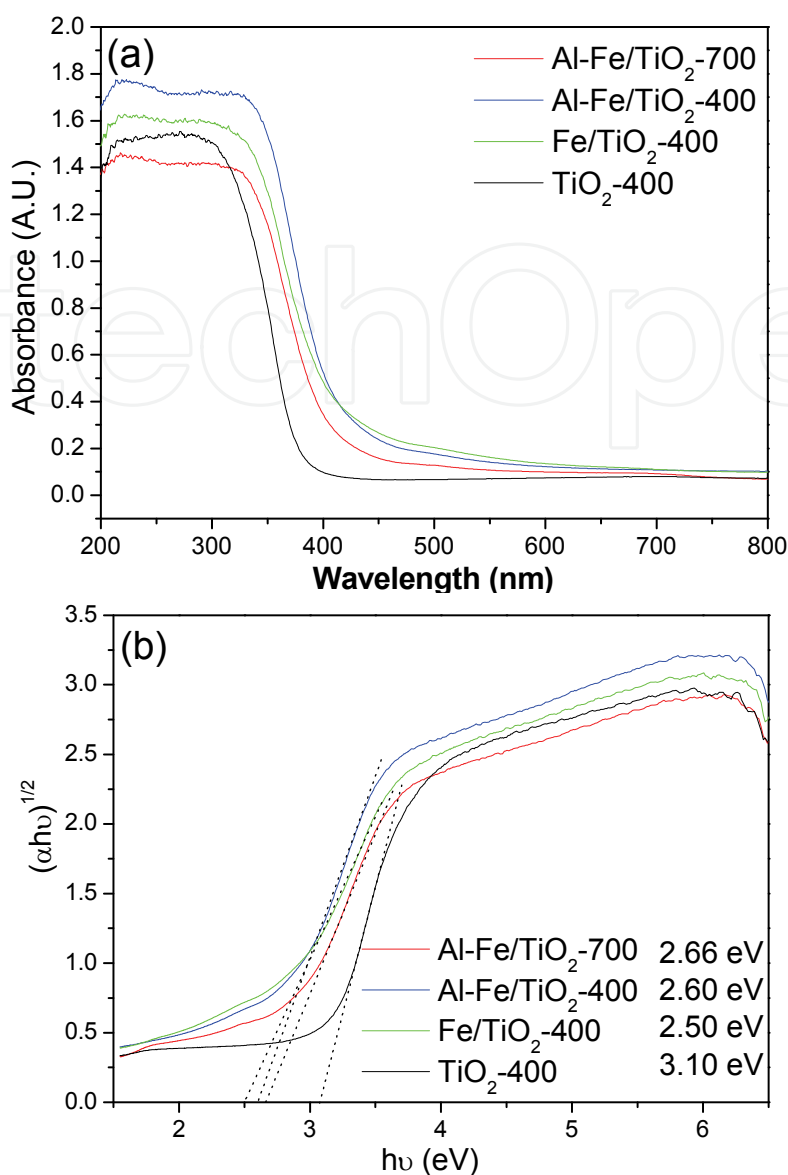
Fig. 4. UV-visible absorption spectra of (a) and determination of indirect interband transition energies (b) for pure TiO_2, Fe/TiO_2-400, Al-Fe/TiO_2-400, and Al-Fe/TiO_2-700 samples.

sensitization region. However, a very weak blue shift to short wavelength was observed for Al-Fe/TiO_2 sample after 700 °C calcining treatment. The band energy gap of the as-prepared samples could be calculated by using $(\alpha h\nu)^n = k(h\nu - E_g)$, where α is the absorption coefficient, k is the parameter that related to the effective masses associated with the valence and conduction bands, n is $1/2$ for a direct transition, $h\nu$ is the absorption energy, and E_g is the band gap energy.(Li, Zhang et al. 2009) Plotting $(\alpha h\nu)^{1/2}$ versus $h\nu$ based on the spectral response in Figure 4a gave the extrapolated intercept corresponding to the E_g value (see Figure 4b). The optical band energies of the macro/mesoporous TiO_2-400, Fe/TiO_2-400, Al-Fe/TiO_2-400 and Al-$Fe/TiO2$-700 samples (3.10 eV, 2.50 eV, 2.60 eV, and 2.66 eV respectively) exhibit obvious red-shifts with respect to that of TiO_2-400 sample (3.10 eV). The results of this study therefore indicate that the enhanced ability to absorb visible-light of this type of macro/mesoporous Al-Fe/TiO_2 makes it a promising photocatalyst for solar-driven applications.
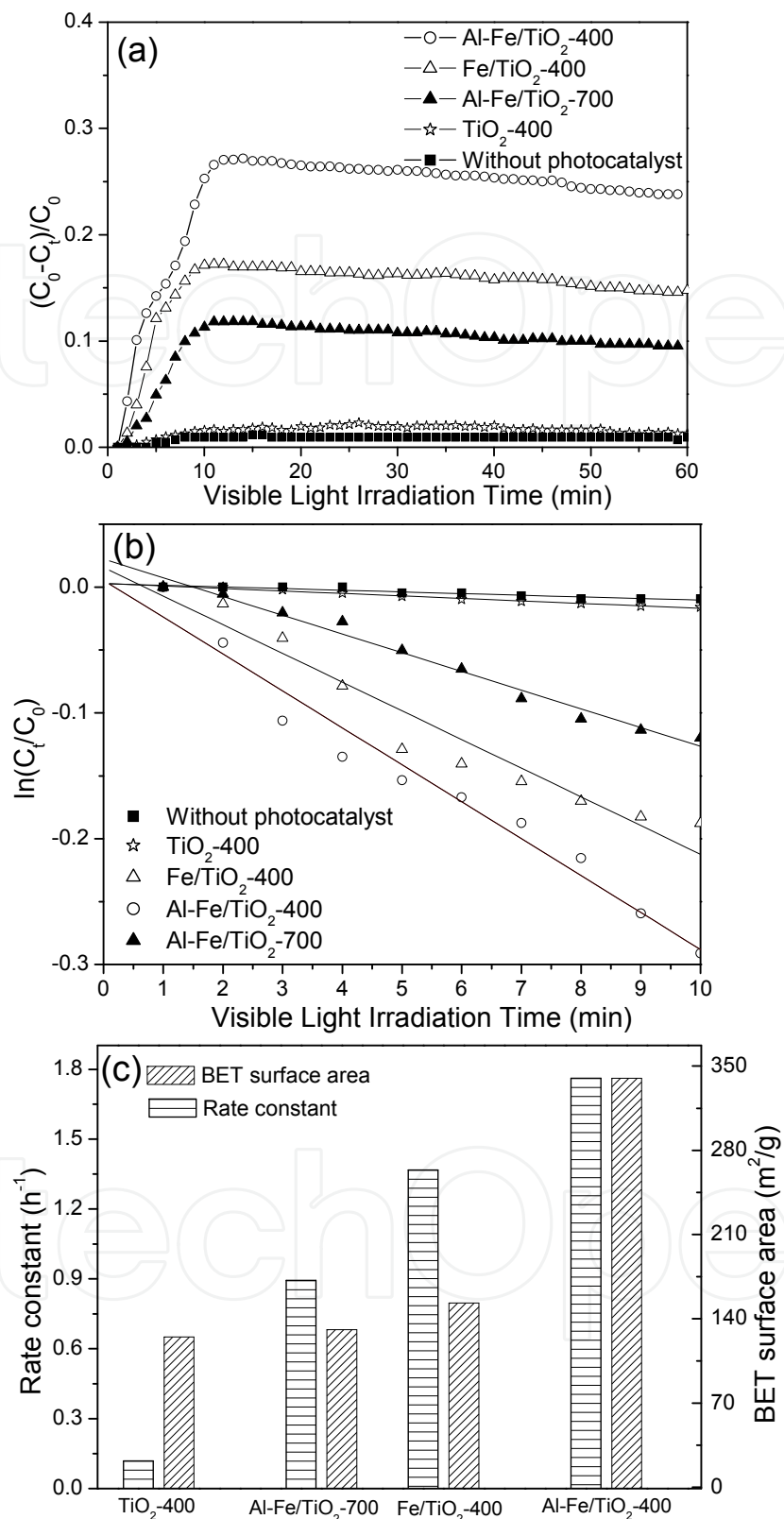
Fig. 5. (a) Plots of the removal of NO concentration vs irradiation time in the presence of the as-prepared products with visible-light irradiation ($\lambda > 400$ nm). (b) Dependence of $\ln(C/C_0)$ on irradiation time. (c) Relationship between rate constant and BET surface area over the as-prepared products.

To evaluate the photocatalytic performance of the as-prepared materials. The photo-oxidation of NO gas under visible light irradiation ($\lambda > 400$ nm) in a single pass flow was used as a photoreaction probe. Figure 5a shows the relative of NO removal rate against irradiation time in the presence of photocatalysts under visible-light irradiation. In the absence of the photocatalyst, no obvious removal rate of NO can be observed. The Photocatalytic performance of pure TiO_2 can be nearly neglected. The NO removal rate over Fe/TiO_2-400 sample reaches 17 % after 20 min irradiation, indicating the promotion effect of Fe-doping. Compared to Fe/TiO_2-400, Al-Fe/TiO_2-400 exhibits a much higher removal rate (about 28 % after 20 min irradiation). Such high photocatalytic performance maybe attributed to the high surface area, large pore volume. Besides, 3D connected pore tunnels are also very important because they can allow the NO molecule to transport very conveniently in the body of the catalyst. Further increasing the calcinations temperature to 700 °C quickly decreased the removal rate to about 10 %.

For a clear quantitative comparison, we use the Langmuir-Hinshelwood model (L-H) to describe the initial rates of photocatalytic removal of NO. The photocatalytic oxidation of NO was recognized to follow a first-order-kinetics approximately as a result of low concentration target pollutants, as evidenced by the linear plot of ln (C/C_0) versus photocatalytic reaction time t (Figure 5b). The rate constants of the TiO_2-400, Fe/TiO_2-400, Al-Fe/TiO_2-400 and Al-Fe/TiO_2-700 samples are 0.119 h^{-1}, 1.368 h^{-1}, 1.762 h^{-1} and 0.893 h^{-1} respectively. Figure 5c shows the relationship between reaction rate constants and BET surface areas. Al-Fe/TiO_2-400 sample owns the highest surface area of 340 m^2/g, resulting in an excellent photocatalytic performance in oxidation of NO. Though the surface area of Al-Fe/TiO_2-700 is similar to that of Fe/TiO_2-400, the reaction rate constant of the formed is much lower that of the latter. Except for the effect of surface area, other factors such as the band gap and light adsorption capability also play an important role in controlling the photocatalytic performance of the catalysts. As shown in Figure 4b, the band gap of Al-Fe/TiO_2-700 is 2.66 eV is higher than that of Fe/TiO_2-400. Meanwhile, the light adsorption intensity of Al-Fe/TiO_2-700 is much lower than that of Fe/TiO_2-400.

4. Conclusions

Macro/mesoporous Fe/TiO_2 was fabricated by soft-chemical synthesis in the presence of surfactants, followed by calcination. Such materials have been proved as a good photocatalyst for treating NO at air conditions for its special macro/mesoporous structures. The modification of Al_2O_3 can effectively increase the thermal stability of Fe/TiO_2 with a very high surface area, resulting in an excellent photocatalytic performance during the oxidation of 400 ppb level of NO in air under visible light irradiation. The present work demonstrates that the hierarchical macro/mesoporous Fe/TiO_2 photocatalysts are effective visible-light-driven photocatalytic functional materials for air purification.

5. Acknowledgments

6. References

Chen, X., Wang, X. & Fu, X. (2009). Hierarchical Macro/Mesoporous TiO$_2$/SiO$_2$ and TiO$_2$/ZrO$_2$ Nanocomposites for Environmental Photocatalysis. Energy & Environmental Science, Vol.2, No.8, (May 2009), pp.872-877, ISSN: 1754-5692

Li, G., Zhang, D. & Yu, J. (2009). Thermally Stable Ordered Mesoporous CeO$_2$/TiO$_2$ Visible-Light Photocatalysts. Physical Chemistry Chemical Physics, Vol.11, No.19, (February 2009), pp.3775-3782, ISSN: 1463-9076

Machida, M., Norimoto, K., Watanabe, T., Hashimoto, K. & Fujishima, A. (1999). The Effect of SiO$_2$ Addition in Super-Hydrophilic Property of TiO$_2$ Photocatalyst. Journal of Materials Science, Vol.34, No.11, (June 1999), pp.2569-2574. ISSN: 0022-2461

Nahar, S., Hasegawa, K. & Kagaya, S. (2006). Photocatalytic Degradation of Phenol by Visible Light-Responsive Iron-Doped TiO$_2$ and Spontaneous Sedimentation of the TiO$_2$ Particles. Chemosphere, Vol.65, No.11, (December 2006), pp.1976-1982. ISSN: 0045-6535

Rolison, D. (2003). Catalytic Nanoarchitectures - The Importance of Nothing and the Unimportance of Periodicity. Science, Vol.299, No.5613, (May 2003), pp.1698-1701. ISSN: 0036-8075

Wang, X., Yu, J., Chen, Y., Wu, L. & Fu, X. (2006). ZrO$_2$-Modified Mesoporous Manocrystalline TiO$_{2-x}$N$_x$ as Efficient Visible Light Photocatalysts. Environmental Science & Technology, Vol,40, No.7, (April 2006), pp.2369-2374, ISSN: 0013-936X

Wang, X., Yu, J., Ho, C., Hou, Y. & Fu, X. (2005). Photocatalytic Activity of a Hierarchically Macro/Mesoporous Titania. Langmuir, Vol.21, No.6, (March 2005), pp.2552-2559, ISSN: 0743-7463

Wu, N., Wang, S. & Rusakova, I. (1999). Inhibition of Crystallite Growth in the Sol-Gel Synthesis of Nanocrystalline Metal Oxides. Science, Vol.285, No.5432, (August 1999), pp.1375-1377, ISSN: 0036-8075

Yu, J., Li, G., Wang, X., Hu, X. Leung, C. & Zhang, Z. (2006). An Ordered Cubic Im3m Mesoporous Cr-TiO$_2$ Visible Light Photocatalyst. Chemical Communications, Vol.25, (September 2006), pp.2717-2719, ISSN: 1359-7345

Yu, J. C., Wang, X., & Fu, X. (2004). Pore-Wall Chemistry and Photocatalytic Activity of Mesoporous Titania Molecular Sieve Films. Chemistry of Materials, Vol.16, No.8, (April 2004), pp.1523-1530, ISSN: 0897-4756

Yuan, Z. &. Su, L. (2006). Insights into Hierarchically Meso-Macroporous Structured Materials. Journal of Materials Chemistry, Vol.16, No.7, (Febrary2006), pp.663-677, ISSN: 0959-9428

Zhu, J., Ren, J., Huo, Y., Bian, Z. & Li, H. (2007). Nanocrystalline Fe/TiO$_2$ Visible Photocatalyst with a Mesoporous Structure Prepared via a Nonhydrolytic Sol-Gel Route. Journal of Physical Chemistry C, Vol.111, No.51, (December 2007), pp.18965-18969, ISSN: 1932-7447
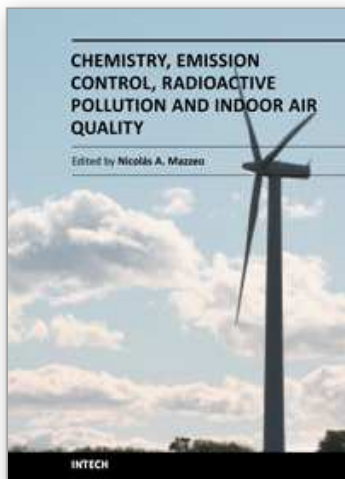
Chemistry, Emission Control, Radioactive Pollution and Indoor Air Quality

Edited by Dr. Nicolas Mazzeo

The atmosphere may be our most precious resource. Accordingly, the balance between its use and protection is a high priority for our civilization. While many of us would consider air pollution to be an issue that the modern world has resolved to a greater extent, it still appears to have considerable influence on the global environment. In many countries with ambitious economic growth targets the acceptable levels of air pollution have been transgressed. Serious respiratory disease related problems have been identified with both indoor and outdoor pollution throughout the world. The 25 chapters of this book deal with several air pollution issues grouped into the following sections: a) air pollution chemistry; b) air pollutant emission control; c) radioactive pollution and d) indoor air quality.

How to reference

In order to correctly reference this scholarly work, feel free to copy and paste the following:

Dieqing Zhang and Guisheng Li (2011). Al2O3-enhanced Macro/Mesoporous Fe/TiO2 for Breaking Down Nitric Oxide, Chemistry, Emission Control, Radioactive Pollution and Indoor Air Quality, Dr. Nicolas Mazzeo (Ed.), ISBN: 978-953-307-316-3, InTech, Available from: http://www.intechopen.com/books/chemistry-emission-control-radioactive-pollution-and-indoor-air-quality/al2o3-enhanced-macro-mesoporous-fe-tio2-for-breaking-down-nitric-oxide

INTECH
open science | open minds